Available online at www.sciencedirect.com

SciVerse ScienceDirect

Nuclear Physics A 881 (2012) 115–126

NUCLEAR PHYSICS A

www.elsevier.com/locate/nuclphysa

Chirally motivated $\bar{K}N$ amplitudes for in-medium applications

A. Cieplý [a,*], J. Smejkal [b]

[a] *Nuclear Physics Institute, 250 68 Řež, Czech Republic*
[b] *Institute of Experimental and Applied Physics, Czech Technical University in Prague, Horská 3a/22, 128 00 Praha 2, Czech Republic*

Received 3 December 2011; received in revised form 31 January 2012; accepted 31 January 2012

Available online 1 February 2012

Abstract

A new fit of a chirally motivated coupled-channel model for meson–baryon interactions is presented including the recent SIDDHARTA data on the 1s level characteristics of kaonic hydrogen. The kaon–nucleon amplitudes generated by the model are fully consistent with our earlier studies. We argue that a sharp increase of the real part of the in-medium $K^- p$ amplitude at subthreshold energies provides a link between the shallow $\bar{K}$–nuclear optical potentials obtained microscopically from threshold $\bar{K}N$ interactions and the phenomenological deep ones deduced from kaonic atoms data. The impact on the A-dependence of the Λ-hypernuclear formation rates measured in reactions with stopped kaons is discussed too.

Keywords: Chiral model; Kaon–nucleon amplitude; Nuclear medium effects; Optical potential; Hypernuclei

1. Introduction

The interaction of kaons with nuclear medium is standardly described in terms of kaon–nuclear optical potential constructed as a coherent sum of kaon interactions with individual nucleons, $V_K(\rho) \sim F_{KN}\rho$, where F_{KN} is the effective elementary kaon–nucleon scattering amplitude and ρ stands for the nuclear density. For many years the strength of the attractive K^-–nuclear optical potential remained a puzzle with two conflicting scenarios. The density dependent formulation of the F_{K^-N} amplitude implemented in phenomenological fits to

* Corresponding author.
E-mail address: cieply@ujf.cas.cz (A. Cieplý).

0375-9474/$ – see front matter
doi:10.1016/j.nuclphysa.2012.01.028

kaonic atoms data gave a strong evidence of a deep K^-–nuclear potential [1], in the range $\mathrm{Re}\, V_{K^-}(\rho_0) \sim -(150\text{–}200)$ MeV at nuclear density $\rho_0 = 0.17$ fm^{-3}. On the other hand, models based on a threshold value of the $\bar{K}N$ amplitude calculated within coupled-channel $\pi\Sigma$–$\bar{K}N$ framework with chiral dynamics [2–5] provide an optical potential which is only (40–50) MeV deep when nuclear medium effects (Pauli blocking and kaon self-energy) are taken into account [6,7]. In a recent work [8] its authors pointed to a strong energy dependence of the chirally motivated in-medium K^-p amplitude and suggested that the puzzling discrepancy could be resolved by evaluating the amplitude at subthreshold energies rather than at the $\bar{K}N$ threshold.

In the present paper we demonstrate that the subthreshold energy dependence of the K^-p interaction depends only moderately on particularities of the underlying chiral model. Specifically, we show that our new fits of model parameters to the fresh experimental data on kaonic hydrogen characteristics [9] generate $\bar{K}N$ amplitudes that are quite consistent with those obtained with a model [10] fitted to the older kaonic hydrogen data [11]. We also present the $\pi\Sigma$ mass spectrum generated by the model that appears consistent with observations of the $\Lambda(1405)$ resonance peaking at energies around 1400 MeV, rather then around 1420 as advocated by some other authors [12,13]. Finally, we briefly review the impact of energy dependence implemented in evaluation of K^-N branching ratios on the calculated Λ-hypernuclear formation rates in the $(K^-_{\mathrm{stop}}, \pi^-)$ reactions [14,15].

2. Separable potentials model

The synergy of chiral perturbation theory and coupled-channel T-matrix re-summation techniques provides successful description of $\bar{K}N$ interactions at low energies. In our approach we employ chirally motivated coupled-channel s-wave potentials that are taken in a separable form,

$$V_{ij}\big(p, p'; \sqrt{s}\big) = \sqrt{\frac{1}{2\omega_i}\frac{M_i}{E_i}}\, g_i(p)\, \frac{C_{ij}(\sqrt{s})}{f_i\, f_j}\, g_j\big(p'\big) \sqrt{\frac{1}{2\omega_j}\frac{M_j}{E_j}}, \tag{1}$$

with $\sqrt{s}$, p and p' denoting the total meson–baryon center-of-mass energy, initial and final state meson momenta, respectively. Further, E_i, M_i and ω_i stand for the baryon energy, baryon mass and meson energy in the c.m. system of channel i. The coupling matrix C_{ij} is determined by chiral SU(3) symmetry. The parameters f_i represent the pseudo-scalar meson decay constants and the Yamaguchi type form factors $g_i(p) = 1/[1 + (p/\alpha_i)^2]$ are determined by inverse range parameters α_i. The indices i and j run over the meson–baryon coupled channels $\pi\Lambda$, $\pi\Sigma$, $\bar{K}N$, $\eta\Lambda$, $\eta\Sigma$ and $K\Xi$, including all their appropriate charge states. Details of the model are given in Ref. [10] where a common value of $f_i = f \sim 100$ MeV was adopted in all channels and used as a free parameter in fits to experimental data. Here we follow the example of Refs. [16] and [17] and allow for three different couplings f_π, f_K and f_η.

The chiral symmetry of meson–baryon interactions is reflected in the structure of the C_{ij} coefficients derived directly from the Lagrangian. In practice, one often considers only the leading order Tomozawa–Weinberg (TW) interaction with energy dependence given by

$$C_{ij}(\sqrt{s}) = -C^{\mathrm{TW}}_{ij}(2\sqrt{s} - M_i - M_j)/4, \tag{2}$$

with C^{TW}_{ij} standing for the SU(3) Clebsh–Gordan coefficients. The exact content of the matrix elements up to second order in the meson c.m. kinetic energies was already specified in Ref. [2] and followed in Ref. [10]. In the present work we adopt an alternate formulation of

the next-to-leading order (NLO) terms for the s-type (direct) and u-type (crossed) Born amplitudes. Following the prescription for these two terms by N. Fettes [18,19] and keeping only the contributions up to second order in meson momenta the two NLO terms read

$$C_{ij}^{(s)}(\sqrt{s}) = 0,$$
$$C_{ij}^{(u)}(\sqrt{s}) = C_{ij}^{(u)} \frac{1}{M_0}\left(-p_i^2 - p_j^2 + \frac{1}{3}\frac{p_i^2 p_j^2}{m_i m_j}\right), \tag{3}$$

where the coefficients $C_{ij}^{(u)}$ are the same as those specified in Table 11 of Ref. [10], M_0 stands for the baryon mass in the chiral limit and m_i denote the meson masses. The main advantages of the adopted formulation are a scalar character of the baryon propagator and its angular independence in case of the u-term. The vanishing of the s-term appears due to averaging over angles in the s-wave and would not occur if our model involved higher angular momenta. The resulting form of our u-term requires additional comments. In a proper NLO expansion, there should be a product of meson energies ω_i and ω_j in the denominator of the last contribution instead of the masses m_i and m_j. However, this would make the u-term divergent for very deep subthreshold energies where $p_i^2 \sim -m_i^2$. This would lead to unphysical divergences in our meson–baryon interaction potential (1) that should be cured by higher than NLO terms. Since we terminate the chiral expansion at the second order we have to regularize the u-term in some other way which we do by approximating the meson energies there by their masses. We have checked that this approximation is perfectly justified in a large energy interval around the $\bar{K}N$ threshold, without any observable impact on the resulting $\bar{K}N$ amplitudes as far as to $\pi\Sigma$ threshold when extrapolating to $\bar{K}N$ subthreshold energies.

When the separable potentials (1) are used in coupled-channel Lippman–Schwinger equation the resulting scattering amplitudes are also of a separable form given explicitly by

$$F_{ij}(p, p'; \sqrt{s}) = -\frac{g_i(p) g_j(p')}{4\pi f_i f_j}\sqrt{\frac{M_i M_j}{s}}\left[\left(1 - C(\sqrt{s})\cdot G(\sqrt{s})\right)^{-1}\cdot C(\sqrt{s})\right]_{ij}. \tag{4}$$

Here the meson–baryon propagator $G(\sqrt{s})$ is diagonal in the channel indices i and j. When the elementary $\bar{K}N$ system is submerged in the nuclear medium one has to consider Pauli blocking and self-energies (SE) generated by the interactions of mesons and baryons with the medium. Thus, the propagator $G(\sqrt{s})$ and the amplitudes F_{ij} become dependent on the nuclear density ρ. The intermediate state Green's function is calculated as

$$G_i(\sqrt{s}; \rho) = \frac{1}{f_i^2}\frac{M_i}{\sqrt{s}}\int\limits_{\Omega_i(\rho)} \frac{d^3\vec{p}}{(2\pi)^3}\frac{g_i^2(p)}{p_i^2 - p^2 - \Pi_i(\sqrt{s}, \vec{p}; \rho) + \mathrm{i}0}, \tag{5}$$

where $\vec{p}_i$ is the on-shell c.m. momentum in channel i and the integration domain $\Omega_i(\rho)$ is limited by the Pauli principle in the $\bar{K}N$ channels. Included in the denominator of the Green's function (5) is the sum Π_i of meson and baryon self-energies in channel i. Since the kaon SE is constructed from the resulting $\bar{K}N$ amplitudes a selfconsistent procedure is required as first suggested by Lutz [20]. In our calculation, following Ref. [7], the baryon and pion self-energies were approximated by momentum independent potentials $V = V_0\,\rho/\rho_0$ with real and imaginary parts of V_0 chosen consistently from mean-field potentials used in nuclear structure calculations and in scattering calculations, respectively. Specifically, we adopted $V_0^{\pi} = (30 - \mathrm{i}10)$ MeV, $V_0^{\Lambda} = (-30 - \mathrm{i}10)$ MeV, $V_0^{\Sigma} = (30 - \mathrm{i}10)$ MeV and $V_0^{N} = (-60 - \mathrm{i}10)$ MeV.

2.1. Fits to experimental data

The free parameters of the separable-interaction chiral models considered in Ref. [10] and in the present work were fitted to the available experimental data on low energy $\bar{K}N$ interactions consisting of

- the $K^- p$ cross sections for the elastic scattering and reactions (see references collected in [2]); following the procedure adopted in [10] we consider only the data points at the kaon laboratory momenta $p_{LAB} = 110$ MeV (for the $K^- p$, $\bar{K}^0 n$, $\pi^+ \Sigma^-$, $\pi^- \Sigma^+$ final states) and at $p_{LAB} = 200$ MeV (for the same four channels plus $\pi^0 \Lambda$ and $\pi^0 \Sigma^0$);
- the $K^- p$ threshold branching ratios, standardly denoted as γ, R_c, and R_n [21];
- the kaonic hydrogen characteristics, the strong interaction shift of the $1s$ energy level ΔE_{1s} and the decay width of the $1s$ level Γ_{1s} provided by the recent SIDDHARTA measurement [9]; the older DEAR data [11] were used in Ref. [10].

In general, the chirally motivated models have no problem with reproduction of the low energy $K^- p$ cross sections, mostly due to relatively large error bars of the experimental data. This goes in line with inclusion of the data taken only at two representative kaon momenta to fix the cross section magnitude, which turns out sufficient for a good reproduction of the experimental cross sections in the whole low energy region [10]. The threshold branching ratios are determined with much better precision and provide a sterner test for any quantitative usage of the models. Another stringent test is provided by the new SIDDHARTA measurement [9] of the kaonic hydrogen data which appears consistent with the other older data [21] on the $K^- p$ reactions at threshold and low energies.

In the current work we present results of two fits to the experimental data, one performed with only the leading order (LO) Tomozawa–Weinberg interaction (2) which we denote TW1, and another one that includes the other first order plus second order corrections as well and will be referred to as NLO30. Since we fit only 15 experimental data (10 cross sections, 3 branching ratios, 2 kaonic hydrogen characteristics) it is essential to reduce the number of free parameters as much as possible. Our TW1 fit was obtained by varying only one inverse range parameter common to all channels, $\alpha_i = \alpha_{TW} = 701$ MeV, and one meson decay constant, $f_i = f_{TW} = 113$ MeV. For the NLO30 fit we fixed the couplings f_i at their physical values $f_\pi = 92.4$ MeV, $f_K = 110.0$ and $f_\eta = 118.8$ MeV (see references cited in [17]), and the inverse ranges of the channels closed at the $\bar{K}N$ threshold were set to $\alpha_{\eta\Lambda} = \alpha_{\eta\Sigma^0} = \alpha_{K\Xi} = 700$ MeV. The remaining three inverse ranges $\alpha_{\pi\Lambda}$, $\alpha_{\pi\Sigma}$ and $\alpha_{\bar{K}N}$ were varied together with four low energy constants (denoted as d's, see Ref. [10] for their specification) of the second order chiral Lagrangian. The remaining low energy constants (couplings of the second order chiral Lagrangian, parameters $b_D = 0.064$ GeV^{-1}, $b_F = -0.209$ GeV^{-1}) were fixed to satisfy the Gell-Mann formulas for baryon mass splittings, to give the pion–nucleon sigma term $\sigma_{\pi N} = 30$ MeV (parameter $b_0 = -0.190$ GeV^{-1}) and to reproduce the semileptonic hyperon decays (parameters $D = 0.80$, $F = 0.46$) [10]. Thus, the NLO30 model has only 7 free parameters fitted to the data while 10 free parameters were used in our earlier work [10] and even more of them were employed in Ref. [17]. Finally, we note that unlike in Ref. [10] we keep the energy dependence of the TW term in the same form as in our TW1 fit, Eq. (2). This correction as well as a use of empirical PS meson decay constants introduce additional chiral symmetry breaking effects that can be viewed as renormalization of the pertinent chiral Lagrangian quantities, thus reducing impact of higher orders in the chiral expansion. In Ref. [8] our TW1 model was already discussed and used in analysis of kaonic atoms and

Table 1
$K^- p$ threshold data calculated in several LO and LO + NLO coupled-channel chiral models. The columns show the kaonic hydrogen 1s level shift ΔE_{1s} and width Γ_{1s} (in eV; the values marked by an asterisk were derived from the $K^- p$ scattering length by means of the modified Deser–Trueman formula [22]), and the $K^- p$ threshold branching ratios γ, R_c, R_n. The last two columns list the $I = 0$ S-matrix pole positions z_1, z_2 (in MeV) related to the $\Lambda(1405)$ resonance. The last two lines show the experimental data and their errors.

Model	ΔE_{1s}	Γ_{1s}	γ	R_c	R_n	z_1	z_2
TW1	323	659	2.36	0.636	0.183	(1371, −54)	(1433, −25)
TW2 [3]	275*	586*	2.30	0.618	0.257	(1389, −64)	(1427, −17)
TW3 [17]	373*	495*	2.36	0.66	0.20	(1384, −90)	(1422, −16)
NLO30	310	607	2.37	0.660	0.191	(1355, −86)	(1418, −44)
CS30 [10]	260	692	2.37	0.655	0.188	(1398, −51)	(1441, −76)
BNW [4]	236*	580*	2.35	0.653	0.194	(1408, −37)	(1449, −106)
IHW [17]	306*	591*	2.37	0.66	0.19	(1381, −81)	(1424, −26)
Exp.	283	541	2.36	0.664	0.189	–	–
Error (±)	42	111	0.04	0.011	0.015	–	–

kaon–nuclear quasi-bound states alongside with an older NLO model CS30 taken from Ref. [10]. Since the CS30 model was fitted to the older DEAR data [11] on kaonic hydrogen it is important to check how much are our conclusions sensitive to the mentioned modifications of the NLO model and to the new experimental data from SIDDHARTA [9].

In Table 1 we show how our TW1 and NLO30 models compare with other models in reproduction of the $\bar{K}N$ threshold data. The first three lines are reserved for models that implement only the TW interaction, the next four lines for representative examples of models that incorporate all LO and NLO terms. Only the present and the models from Ref. [17] use the new SIDDHARTA measurement [9] of kaonic hydrogen characteristics while the CS30 [10] and BNW [4] models were fitted to the DEAR data [11]. The model of Ref. [3] was fitted only to the threshold branching ratios and to the shape of the $\Lambda(1405)$ resonance in the $\pi\Sigma$ mass spectrum. It can be seen that the threshold data are quite well reproduced with the models that are based only on the TW interaction. When we incorporate the NLO terms the total χ^2 per data point drops significantly from 3.6 to 0.61 for the TW1 and NLO30 models, respectively. The CS30 model gives $\chi^2/N = 0.78$ for the data set which includes the new SIDDHARTA measurement. When the parameters of the CS30 model were fitted to the DEAR data [11] the resulting $\chi^2/N = 1.3$ was almost twice as large. This difference demonstrates that the new kaonic hydrogen data [9] from the SIDDHARTA Collaboration are much more consistent with the other low energy data on $K^- p$ scattering and reactions. The two parameter sets of our CS30 and NLO30 models (both of them giving $\sigma_{\pi N} = 30$ MeV) are compared in Table 2. As expected, the alternate treatment of the NLO terms and use of empirical couplings f_i has significant impact on the d-couplings while the inverse ranges α_i are varied only moderately. We also note that our d-couplings are somewhat larger than those reported for the IHW model [17], though there is no simple relation between their and our NLO low energy constants.

The separate treatment of the inverse ranges in different channels and a relatively small value of $\alpha_{\pi\Lambda}$ in our NLO models may require a comment. First of all we note that only a small part of the improvement observed when going from the LO to the NLO30 fit is due to the separate treatment of the inverse ranges in the NLO30 model. In a complementary NLO fit with f_i fixed at physical couplings and only one value of inverse range used in all channels and varied together with the NLO d-couplings the fit to the data gave $\chi^2/N = 1.1$ for $\alpha_i = \alpha_{NLO} = 481$ MeV. Although the quality of this fit is quite good in general it is lacking in respect to the resulting kaonic

Table 2
The inverse ranges (in MeV) and low energy constants d_0, d_D, d_F and d_1 (in GeV^{-1}) fitted to the available K^-p data at threshold and low energies.

Model	$\alpha_{\pi\Lambda}$	$\alpha_{\pi\Sigma}$	$\alpha_{\bar{K}N}$	d_0	d_D	d_F	d_1
CS30	291	601	639	−0.450	0.026	−0.601	0.235
NLO30	297	491	700	−0.812	0.288	−0.737	−0.016

hydrogen $1s$ level width $\Gamma_{1s} = 763$ eV, which is by about two standard deviations larger than the SIDDHARTA value (the energy shift $\Delta E_{1s} = 275$ eV would be fine). The independent variation of inverse ranges in channels open at the $\bar{K}N$ threshold allows to remedy this nuisance. It is also a common practice in other $\bar{K}N$ chiral models [3,4,17] to use channel dependent subtraction constants to regularize the intermediate state integral. The large negative values of the $\pi\Lambda$ subtraction constant reported in the NLO fits of Refs. [4] and [17] are equivalent to a very small cutoff momenta [23] which in turn implies small values of inverse ranges when the intermediate state integral is regularized by means of the Yamaguchi formfactors. Thus, although the relation of our inverse ranges to the subtraction constants is highly nontrivial, the small value of $\alpha_{\pi\Lambda}$ appears in qualitative agreement with the values of the pertinent subtraction constant obtained in other NLO fits of the K^-p data.

Finally, we would like to emphasize the importance of calculating the kaonic hydrogen characteristics directly by solving the kaon–proton bound state problem rather then deriving them from the K^-p elastic amplitude extrapolated to the threshold. Standardly, the kaonic hydrogen shift ΔE_{1s} and width Γ_{1s} are derived from the K^-p scattering length a_{K^-p} by means of a modified Deser–Trueman formula [22] taken to the second order in a_{K^-p}. However, we have shown [5] that the precision of the relation is on a level of 10%. Since the experimental precision of kaonic hydrogen characteristics is getting close to this level one should either expand the relation reported in Ref. [22] to higher orders of a_{K^-p} or solve the K^-p bound state problem numerically as we do here and in Refs. [5] and [10].

Also listed in Table 1 are the positions z_1, z_2 of the two $I = 0$ S-matrix poles that reside on the second Riemann sheet $[-,+]$ of the complex energy manifold, where the signs are those of the imaginary parts of the c.m. momenta in the $\pi\Sigma$ and $\bar{K}N$ channels, respectively. It is remarkable that all the TW models listed in the table are in a relatively close agreement on the position of the upper pole z_2. This agreement is spoiled, at least in our model (unlike in Ref. [17]), when the NLO corrections are included in the inter-channel couplings. In contrast, the position of the lower pole z_1 exhibits model dependence already in the TW models. Generally, it is located much further away from the real axis than the pole z_2. The pole z_2 is usually relegated to the subthreshold behavior of the K^-p amplitude and to the $\Lambda(1405)$ resonance observed in the $\pi\Sigma$ mass spectrum in $\bar{K}N$ initiated reactions.

Fig. 1 visualizes the $\pi\Sigma$ mass distribution computed for the NLO30 model. The solid curve was obtained by tuning the relative couplings of the $\pi\Sigma$ and the $\bar{K}N$ channels to an $I = 0$ source to get a peak at 1395 MeV, see also Refs. [23] and [10] for details. Just for a reference we also show the spectra obtained by assuming that the $I = 0$ resonance originates only from the $\pi\Sigma$ channels (dashed line in Fig. 1) or that it is formed exclusively from the $\bar{K}N$ channels (dotted line). These two lines represent a kind of boundaries on the shape and peak position of the spectra in a situation when the low energy constants are fixed at the values obtained in our NLO30 fit. The experimental data shown in Fig. 1 come from three different measurements [24–26], all exhibiting a prominent structure around 1400 MeV. As the observed spectra are not

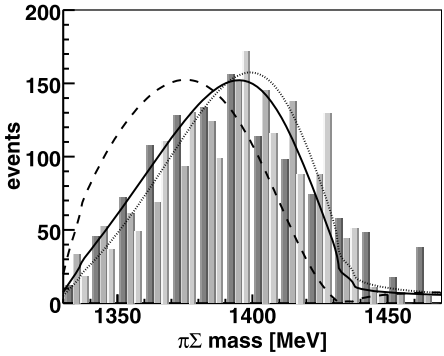

Fig. 1. The $\pi\Sigma$ mass distribution. Our results are compared with the experimental data taken from Refs. [24–26] with the experimental bars at each energy shown in this order. See the text for explanation on the theoretical curves obtained with the NLO30 model.

normalized we have rescaled the original data as well as our computed distributions to give 1000 events in the chosen energy interval (from 1330 to 1440 MeV). The three measurements give $\pi\Sigma$ distributions that look mutually compatible. However, as the experimental spectra contain admixtures of $I = 1$ and $I = 2$ contributions they cannot be compared simply with our theoretical predictions based on an idea of the $I = 0$ source. In reality, a meaningful comparison of the measured $\pi\Sigma$ spectra with theory would also require a proper treatment of the dynamics and kinematics of the particular reaction, i.e. an application of an appropriate reaction model. Since this is out of scope of the present work the comparison of the theoretical and experimental data is presented in Fig. 1 only for illustration. We also mention that the $K^- p \to \Sigma^0\pi^0\pi^0$ data measured by the Crystal Ball Collaboration [27], which are not shown in the figure, yield a slightly different distribution with a peak structure around 1420 MeV. The two identical pions in the final state of this reaction complicate a direct comparison with the other experiments, so we also find it questionable to relate our computed line-shape to the one observed in [27].

2.2. Free space and in-medium $\bar{K}N$ amplitudes

The energy dependence of the $K^- N$ amplitudes in vacuum and in nuclear medium was already discussed extensively in Ref. [8] where the reduced amplitudes (stripped off the form factors g_i) were presented. Here we prefer to show the full on-shell amplitude $F_{\bar{K}N}$ and anticipate purely imaginary momenta $p_{\bar{K}N} = \mathrm{i}|p_{\bar{K}N}|$ for the subthreshold energies. In the present Fig. 2 we compare the energy dependence of the elastic $K^- p$ amplitude in the free space as generated by three different models. The pronounced peak in $\mathrm{Im}\, F_{K^- p}$ and the change of sign in $\mathrm{Re}\, F_{K^- p}$ point to the existence of a quasi-bound state related to the $\Lambda(1405)$ resonance closely below the $K^- p$ threshold. This feature is common to all models based on chiral dynamics which, in combination with couple channel re-summation, generate the resonance dynamically. The three models employed in our calculations lead to very similar $\bar{K}N$ amplitudes above the threshold and are in qualitative agreement at subthreshold energies as well. Interestingly, Fig. 2 also demonstrates that the NLO30 model fitted to the SIDDHARTA data [9] leads to $K^- p$ amplitudes that are in close agreement with those obtained for the CS30 model fitted to the DEAR data [11]. Especially, the real parts of the amplitudes generated by the CS30 and NLO30 models are very close to each other when extrapolated as far as to (and even below) the $\pi\Sigma$ threshold. This feature may be explained by recalling that in fact the CS30 model was not able to reproduce the DEAR data and

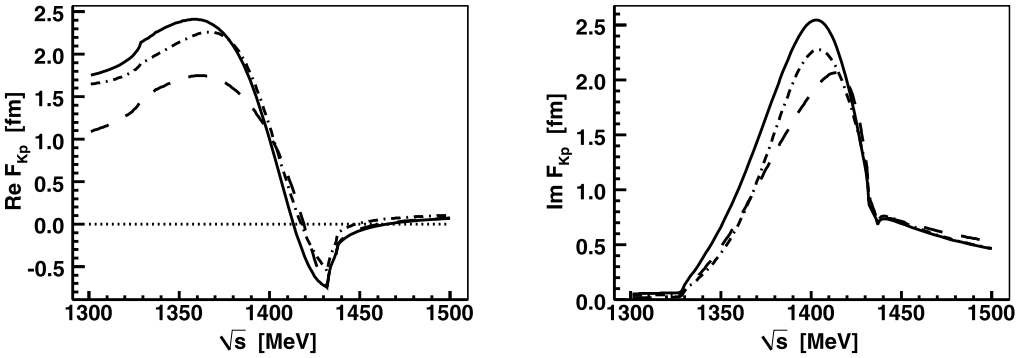

Fig. 2. Energy dependence of the real (left panel) and imaginary (right panel) parts of the elastic $K^- p$ amplitude in the free space. Dashed curves: TW1 model, dot-dashed: CS30 model, solid curves: NLO30 model.

generates kaonic hydrogen characteristics that are more compatible with the SIDDHARTA results. In other words, the energy dependence of the $K^- p$ amplitude is to some extent fixed by the very precise threshold branching ratios and by the low energy scattering and reaction data (see Ref. [28] for a detailed analysis). The significance of the new SIDDHARTA data can be judged in terms of putting additional constrains on the models and reducing the theoretical uncertainties when extrapolating the $\bar{K}N$ interaction to subthreshold energies [17].

Another point worth mentioning is related to the positions of the poles of the S-matrix shown in Table 1. Standardly, the threshold behavior of the $K^- p$ amplitude is viewed as strongly affected by the higher of the $I = 0$ poles, here labeled as z_2. We note that this pole is located at rather varied positions for the three different models depicted in Fig. 2. For our CS30 model the z_2 pole is found even above the $\bar{K}N$ threshold and further from the real axis, so it might be the lower z_1 pole that affects more the subthreshold $K^- p$ interaction in this case. Since all our models lead to very similar $K^- p$ amplitudes at energies at and above the threshold, it looks that the positions of the $I = 0$ poles cannot be unambiguously determined from the current experimental data. In this respect our observation is similar to the one made by Shevchenko [29] who arrived at a conclusion that the available experimental data can be described equally well by models that incorporate either one or two $I = 0$ poles.

In Fig. 3 we show the energy dependence of the elastic $K^- p$ amplitude in nuclear medium for the nuclear density $\rho = \rho_0$. Both the Pauli blocking as well as the meson and baryon self-energies were included when computing the amplitudes in a selfconsistent way. Standardly, only 5–10 iterations are required to achieve the selfconsistency [7]. The qualitative behavior of the amplitudes is once again independent of the model used in the calculations. It is remarkable that the selfconsistent treatment leads to even smaller differences between the CS30 and NLO30 models than they were in the free space, especially in the subthreshold energy region. However, the prominent subthreshold increase of in-medium $\bar{K}N$ attraction was not observed in earlier in-medium calculations [6] which get substantially different results than ours already when only Pauli blocking is accounted for. At the moment we have no real explanation for the difference, maybe the on-shell treatment of the intermediate state propagator used in Ref. [6] is not so well justified when the $\bar{K}N$ system is submerged in nuclear medium. On the other hand, we were able to reconstruct fully the results of Ref. [30] (obtained without accounting for the hadron self-energies) when we switched to their parameter set.

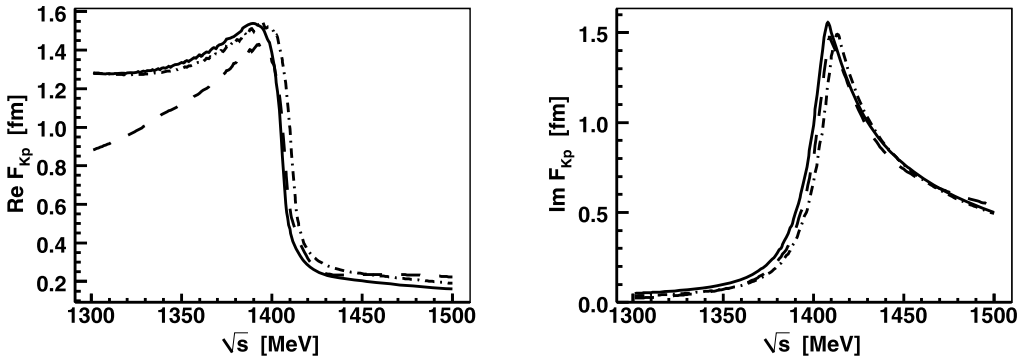

Fig. 3. Energy dependence of the real (left panel) and imaginary (right panel) parts of the elastic $K^- p$ amplitude in nuclear medium at the nuclear density $\rho = \rho_0$. Dashed curves: TW1 model, dot-dashed: CS30 model, solid curves: NLO30 model.

As was already demonstrated in Ref. [8] the in-medium dynamics of the $\Lambda(1405)$ resonance is responsible for the rapid increase of the real part of our $K^- p$ amplitude at energies about 30 MeV below the $\bar{K}N$ threshold. While the Pauli blocking pushes the resonance structure above the threshold the kaon self-energy is responsible for moving it back to energies where it is located in the free space. However, when the nuclear density is increased the relevant $I = 0$ pole crosses the real axis above the $\bar{K}N$ threshold, thus moving to the $[+,-]$ Riemann sheet. Since it is now located much further from the physical region (on a Riemann sheet not connected with the physical one) the $K^- p$ amplitude no longer exhibits the resonance structure characterized by real part of the amplitude crossing zero and imaginary part resembling the Gaussian shape.

Finally, we mention that the free-space $K^- n$ interaction is weakly attractive and its in-medium renormalization is rather weak and exhibits little density dependence [8]. We also note that a proper treatment of the $\bar{K}N$ system submerged in nuclear medium requires an introduction of realistic in-medium $\bar{K}N$ momenta that are used in the Yamaguchi form factors $g_i(p)$ instead of the on-shell momenta assumed in Fig. 3. The details can be found in Ref. [8].

3. Λ-hypernuclear production

As mentioned in Section 1 the energy dependence of the in-medium $\bar{K}N$ amplitudes is crucial for a construction of the kaon–nuclear optical potential. In many applications the $\bar{K}N$ interaction in nuclear medium is probed at energies below the $\bar{K}N$ threshold. The energy shift from threshold to subthreshold energies was estimated in Ref. [8] and an optical potential based on our chirally motivated amplitudes was used there to calculate the bound state characteristics of kaonic atoms and kaon–nuclear quasi-bound states. The energy dependence of the $K^- p$ amplitude shown in Fig. 3 leads to an optical potential that is shallow at the $\bar{K}N$ threshold but becomes much deeper at subthreshold energies relevant for the K^-–nuclear bound state systems. Thus, the shift to subthreshold energies brings the constructed optical potential in agreement with phenomenological analysis of kaonic atoms data that favors deep optical potential [1]. In this section we demonstrate another effect of the in-medium energy dependence that stems from the energy dependence of the $K^- N$ branching ratios.

The new experimental data [14] on the Λ-hypernuclear production in $(K^-_{\rm stop}, \pi^-)$ reactions allow to study the A-dependence of the formation rates for the p-shell nuclear targets. The cal-

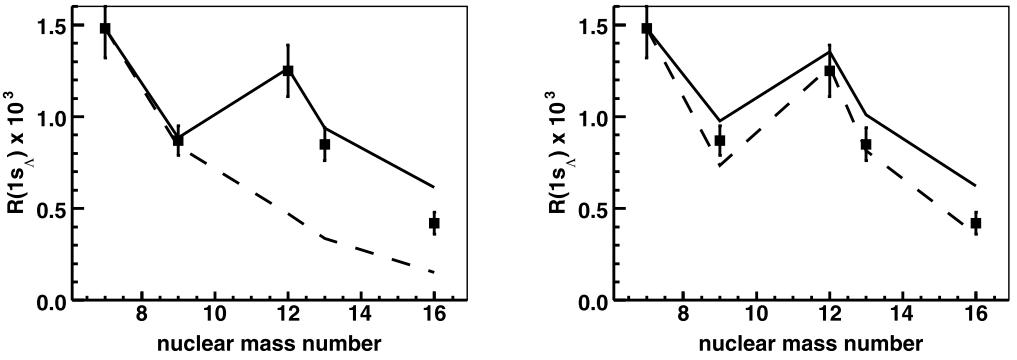

Fig. 4. The A-dependence of the $1s_\Lambda$ hypernuclear formation rates, experimental data by the FINUDA Collaboration [14]. The theoretical rates [15] are normalized to the ^{7}Li experimental value and were calculated with a phenomenological density dependent kaon–nuclear optical potential (dashed lines) and with the chirally motivated K^-–nuclear optical potential (solid lines). Left panel: elementary BR($K^-N \to \pi\Lambda$) fixed at the threshold value for nuclear density $\rho = \rho_0/2$, right panel: energy and density dependent BR.

culated capture rates significantly underestimate the measured ones, the deeper the K^- potential, the smaller is the capture rate [31]. However, one can look at relative rates and the A-dependence of the production rates where the impact of both the theoretical ambiguities and the experimental systematic errors should not obscure our observations [15]. Within a framework of the distorted wave impulse approximation (DWIA) the nuclear capture rate per stopped kaon R_{fi}/K can be expressed as a product of three terms, a kinematic factor, the elementary branching ratio (BR) of the process BR($K^-N \to \pi\Lambda$), and a rate per hyperon R_{fi}/Y [31]. While the BR has standardly been taken as a constant fixed at its threshold value, our work demonstrates the importance of considering the energy and density dependence of the BR.

In Fig. 4 we show the calculated $1s_\Lambda$ formation rates (per stopped kaon) [15] in comparison with the FINUDA data [14] for nuclear targets from ^{7}Li to ^{16}O. The presented theoretical rates were normalized to reproduce exactly the experimental rate for the ^{7}Li target, so one can focus on the A-dependence of the rates. The calculated rates in the left panel of Fig. 4 assume a constant BR generated by the CS30 model, taken at the $\bar{K}N$ threshold and for an intermediate nuclear density $\rho = \rho_0/2$. In this case the A-dependence is solely driven by the rate per hyperon that contains the overlap of the initial and the final state wave functions. There, the chirally motivated kaon–nuclear optical potential (based on the CS30 amplitudes) does a better job than the phenomenological one (based on the density dependent amplitudes from Ref. [1]). The calculated rates presented in the right panel of the figure incorporate in addition the energy and density dependence of the BR that appears due to an energy shift from threshold to subthreshold $\bar{K}N$ energies. Once again we see that the implementation of an energy shift from the $\bar{K}N$ threshold to subthreshold energies (where the in-medium $\bar{K}N$ interaction is effective) significantly alters the observed picture. Both the phenomenological and the chirally motivated optical potentials are sufficiently deep at the subthreshold energies relevant for the evaluation of the energy dependent BR, so they lead to similar $1s_\Lambda$ formation rates.

4. Summary

We have demonstrated that the results of SIDDHARTA experiment [9] on kaonic hydrogen are in good agreement with other available data on K^-p threshold branching ratios and on the

low energy $K^- p$ cross sections. Our new NLO30 model is fully compatible with results of our previous analyses and improves the general description of the data.

The several versions of coupled-channel separable potential models considered in our work provide $\bar{K}N$ amplitudes that exhibit very similar energy dependence in the free space as well as in the nuclear medium. Specifically, the strong subthreshold energy and density dependence of the $K^- p$ amplitudes, that reflects the dominant effect of the $\Lambda(1405)$ resonance, does not depend much on a particular version of the model. The observed sharp increase of $K^- p$ in-medium attraction below the $\bar{K}N$ threshold is a robust feature common to all considered models. It is prominent already in the TW1 model that employs only the leading order TW interaction. The NLO contributions present in the CS30 and NLO30 models improve significantly the quality of the fit to experimental data but their impact on the resulting $\bar{K}N$ amplitudes is only moderate.

Since the K^-–nuclear interaction probes subthreshold $\bar{K}N$ energies where the $K^- p$ in-medium amplitude exhibits much stronger attraction the resulting K^-–nuclear optical potential becomes much deeper than when it were constructed from the amplitudes taken at the $\bar{K}N$ threshold. The mechanism of constructing the optical potential from subthreshold $\bar{K}N$ energies allows to link the shallow $\bar{K}$–nuclear potentials based on the chiral $\bar{K}N$ amplitude evaluated at threshold and the deep phenomenological optical potentials obtained in fits to kaonic atoms data. The relevance of this finding to an analysis of kaonic atoms and quasi-bound $\bar{K}$–nuclear states was already investigated in Ref. [8]. The results are also discussed in separate reports of this journal [32,33].

The subthreshold energy and density dependence of the in-medium elementary branching ratio $\mathrm{BR}(K^- N \to \pi \Lambda)$ has a significant impact on the Λ-hypernuclear production rates observed in reactions with stopped kaons. The implementation of the effect in our DWIA calculations leads to A-dependence of the formation rates that is in very good agreement with the one observed in the FINUDA experiment performed on p-shell nuclear targets. It also brings in agreement the results obtained with K^-–nuclear optical potentials based on either the chirally motivated or the phenomenological density dependent amplitudes. Unfortunately, the magnitude of the computed DWIA rates remains much lower than the rates established experimentally.

Acknowledgements

A.C. acknowledges a fruitful collaboration with E. Friedman, A. Gal, D. Gazda, J. Mareš and V. Krejčiřík who contributed to the papers the current report is partly based on. This work was supported by the Grant Agency of the Czech Republic, Grant No. 202/09/1441. The work of J.S. was also supported by the Research Program Fundamental experiments in the physics of the micro-world, No. 6840770040, of the Ministry of Education, Youth and Sports of the Czech Republic.

References

[1] E. Friedman, A. Gal, C.J. Batty, Nucl. Phys. A 579 (1994) 518–538.
[2] N. Kaiser, P.B. Siegel, W. Weise, Nucl. Phys. A 594 (1995) 325–345.
[3] D. Jido, J.A. Oller, E. Oset, A. Ramos, U.-G. Meißner, Nucl. Phys. A 725 (2003) 181–200.
[4] B. Borasoy, R. Nißler, W. Weise, Eur. Phys. J. A 25 (2005) 79–96.
[5] A. Cieplý, J. Smejkal, Eur. Phys. J. A 34 (2007) 237–241.
[6] A. Ramos, E. Oset, Nucl. Phys. A 671 (2000) 481–502.
[7] A. Cieplý, E. Friedman, A. Gal, J. Mareš, Nucl. Phys. A 696 (2001) 173–193.
[8] A. Cieplý, E. Friedman, A. Gal, D. Gazda, J. Mareš, Phys. Lett. B 702 (2011) 402–407;
A. Cieplý, E. Friedman, A. Gal, D. Gazda, J. Mareš, Phys. Rev. C 84 (2011) 045206.

[9] M. Bazzi, et al., SIDDHARTA Collaboration, Phys. Lett. B 704 (2011) 113–117;
M. Bazzi, et al., SIDDHARTA Collaboration, Nucl. Phys. A 881 (2012) 88–97.
[10] A. Cieplý, J. Smejkal, Eur. Phys. J. A 43 (2010) 191–208.
[11] G. Beer, et al., DEAR Collaboration, Phys. Rev. Lett. 94 (2005) 212302.
[12] V.K. Magas, E. Oset, A. Ramos, Phys. Rev. Lett. 95 (2005) 052301.
[13] T. Hyodo, W. Weise, Phys. Rev. C 77 (2008) 035204.
[14] M. Agnello, et al., FINUDA Collaboration, Phys. Lett. B 698 (2011) 219–225;
M. Agnello, et al., FINUDA Collaboration, Phys. Lett. B 622 (2005) 35–44.
[15] A. Cieplý, E. Friedman, A. Gal, V. Krejčiřík, Phys. Lett. B 698 (2011) 226–230.
[16] J. Nieves, E. Ruiz Arriola, Phys. Rev. D 64 (2001) 116008.
[17] Y. Ikeda, T. Hyodo, W. Weise, Phys. Lett. B 706 (2011) 63–67;
Y. Ikeda, T. Hyodo, W. Weise, Nucl. Phys. A 881 (2012) 98–114.
[18] N. Fettes, Pion nucleon physics in chiral perturbation theory, PhD thesis, Universität Bonn, 2000, Berichte des Forschungszentrums Jülich No. 3814.
[19] N. Fettes, U.-G. Meißner, M. Mojžiš, S. Steininger, Ann. Phys. 283 (2000) 273–307;
N. Fettes, U.-G. Meißner, M. Mojžiš, S. Steininger, Ann. Phys. 288 (2001) 249–250 (Erratum).
[20] M. Lutz, Phys. Lett. B 426 (1998) 12–20.
[21] A.D. Martin, Nucl. Phys. B 179 (1981) 33–48, and references therein.
[22] U.-G. Meißner, U. Raha, A. Rusetsky, Eur. Phys. J. C 35 (2004) 349–357.
[23] J.A. Oller, U.-G. Meißner, Phys. Lett. B 500 (2001) 263–272.
[24] D.W. Thomas, A. Engler, H.E. Fisk, R.W. Kraemer, Nucl. Phys. B 56 (1973) 15–45.
[25] R.J. Hemingway, Nucl. Phys. B 253 (1985) 742–752.
[26] I. Zychor, et al., ANKE Collaboration, Phys. Lett. B 660 (2008) 167–171.
[27] S. Prakhov, et al., Crystal Ball Collaboration, Phys. Rev. C 70 (2004) 034605.
[28] B. Borasoy, U.-G. Meißner, R. Nißler, Phys. Rev. C 74 (2006) 055201.
[29] N.V. Shevchenko, arXiv:1103.4974 [nucl-th].
[30] T. Waas, N. Kaiser, W. Weise, Phys. Lett. B 365 (1996) 12–16.
[31] V. Krejčiřík, A. Cieplý, A. Gal, Phys. Rev. C 82 (2010) 024609.
[32] E. Friedman, A. Gal, Nucl. Phys. A 881 (2012) 150–158.
[33] D. Gazda, J. Mareš, Nucl. Phys. A 881 (2012) 159–168.